ADVANCED MATERIALS INTERFACES
www.advmatinterfaces.de

Spatial Coupling of Ferroelectric Domain Walls and Crystallographic Defects in the $PbTiO_3$ Films

*Ying Liu, Yun-Long Tang, Yin-Lian Zhu, Wen-Yuan Wang, and Xiu-Liang Ma**

Revealing interactions between defects and domain walls is important for understanding the ferroelectric and piezoelectric behaviors of a ferroelectric film, especially when considering the trend of device downscaling. By means of aberration-corrected transmission electron microscopy, domain patterns resulting from the interactions between 90°/180° ferroelectric domain walls and dislocations in the $PbTiO_3$ thin films grown on $SrTiO_3$ are systematically studied. It is found that the coupling of 90° and 180° domain walls with dislocations may induce the formation of 90° charged domain walls and some other novel metastable domain configurations. Such domain patterns are observed to relax with 180° domain walls annihilation and the reversal of polarization directions of *a*- and *c*-domain. The configurations of both dislocations and stacking faults may lead to a dramatic change of the domain patterns. Unusual dislocation strain field is identified for a dislocation with the burgers vector 45° apart from a 90° domain wall. These results provide new insights into the defect and domain wall interactions which are of critical importance for the development of nanoscale devices.

1. Introduction

The oxide interface engineering has attracted increasing interest owing to the emergent phenomena created at the interface, such as 2D electron gas,[1–3] interfacial superconductivity,[4] quantum hall effect,[5] and magnetoelectric coupling.[6,7] Ferroelectric domain walls, which separate domains with different polar directions, are special homogeneous interfaces exhibiting functionalities such as domain wall conductivity[8,9] and photovoltaic effect.[10] However, the ferroelectric and piezoelectric responses of a ferroelectric are greatly influenced by the crystallographic defects in ferroelectric films because they severely impact the field dynamics of domain walls.[11–14] In addition, the interfacial dislocations in ferroelectrics are known to lead to drastic variations of the Curie temperature and polarization distribution near the dislocations.[15–17] Especially, when the sizes of the ferroelectric films are scaling down to the nanoscale, interfacial dislocations could result in polarization instability,[18] and even a single dislocation could decrease the local spontaneous polarization in $PbZr_{0.2}Ti_{0.8}O_3$ film by up to 48%.[19]

In general, much attention has been paid to the interfacial dislocations which deteriorate the properties of a ferroelectric film, such as pinning domain wall and inducing unstable polarization.[18] However, a recent study based on phase-field simulations reveals that dislocation walls in a $PbTiO_3$ (PTO) single crystal not only impact the domain configurations but also improve the ferroelectric properties.[12] These contradictory results indicate that the effects of a dislocation on the domain structures and physical properties of the ferroelectrics are not clarified.

Moreover, although both domain walls and lattice defects are known to have great influences on the properties of a ferroelectric, the detailed interactions between them and the resultant novel phenomena are still less known. In the tetragonal ferroelectrics, previous experimental investigations indicate that misfit dislocations form at film deposition temperature when PTO is cubic with a relatively larger lattice constant compared to $SrTiO_3$(STO), and these dislocations may further promote the nucleation of *a*-domain.[20] However, these studies were mainly concentrated on the interactions between 90° domain walls and dislocations near the heterointerface, where a pair of dislocations with Burgers vector of 1/2*a*[011] were reported in the PTO films grown on a $SrTiO_3$(001) substrate;[20] pairs of dislocations with Burgers vector of *a*[100] and *a*[001] or single dislocation with Burgers vector of *a*[001] were found in the $PbZr_{0.2}Ti_{0.8}O_3$/$SrTiO_3$(001) films;[21,22] *a*[010] dislocations were seen near the $BaTiO_3$/$LaAlO_3$(001) interface.[23] These results indicate that a systematic observation on the interactions between dislocations and 90° domain walls is required. In addition, the effects of 180° or charged domain wall which exhibit little strain were less studied previously due to the lack of instrumental resolution. Although some theoretical calculations about the interaction between dislocations and 90°/180° domain walls have been conducted,[13,14] they are not revealed so far in experiments. Particularly, the atomic details and the local strain interactions were unattainable in these methods.

With the recent development of aberration-corrected (scanning) transmission electron microscope, direct mapping of domain walls at the atomic scale becomes possible.[24–27] For instance, systematic investigations on 180° domain wall[24] and

Dr. Y. Liu, Dr. Y.-L. Tang, Prof. Y.-L. Zhu, Dr. W.-Y. Wang, Prof. X.-L. Ma
Shenyang National Laboratory for Materials Science
Institute of Metal Research
Chinese Academy of Sciences
Wenhua Road 72, 110016 Shenyang, China
E-mail: xlma@imr.ac.cn

DOI: 10.1002/admi.201600342

90° charged domain wall[26] in tetragonal ferroelectrics reveal the different width and polarization characteristics at these domain walls compared to the uncharged one. Nevertheless, spatial coupling between defects and domain wall in PTO film are still not well understood.

In this article, domain patterns and unusual strain state caused by the complex interactions between lattice defects and both 90° and 180° ferroelectric domain walls in PTO films are extensively analyzed on the basis of aberration-corrected scanning transmission electron microscopy (STEM). We find that a specific defect-domain wall interaction may give rise to a metastable domain configuration, such as unstable *a*- and *c*-domain, charged 90° domain walls as well as superdomain patterns. The relaxation of such metastable domain configurations is observed which may induce retention failure. In addition, it is found that 90° domain walls are usually accompanied with specific dislocations. An unusual dislocation strain field which is along 90° domain wall is revealed, which deviates 45° from that of the typical dislocation with $b = a[0\bar{1}0]$.

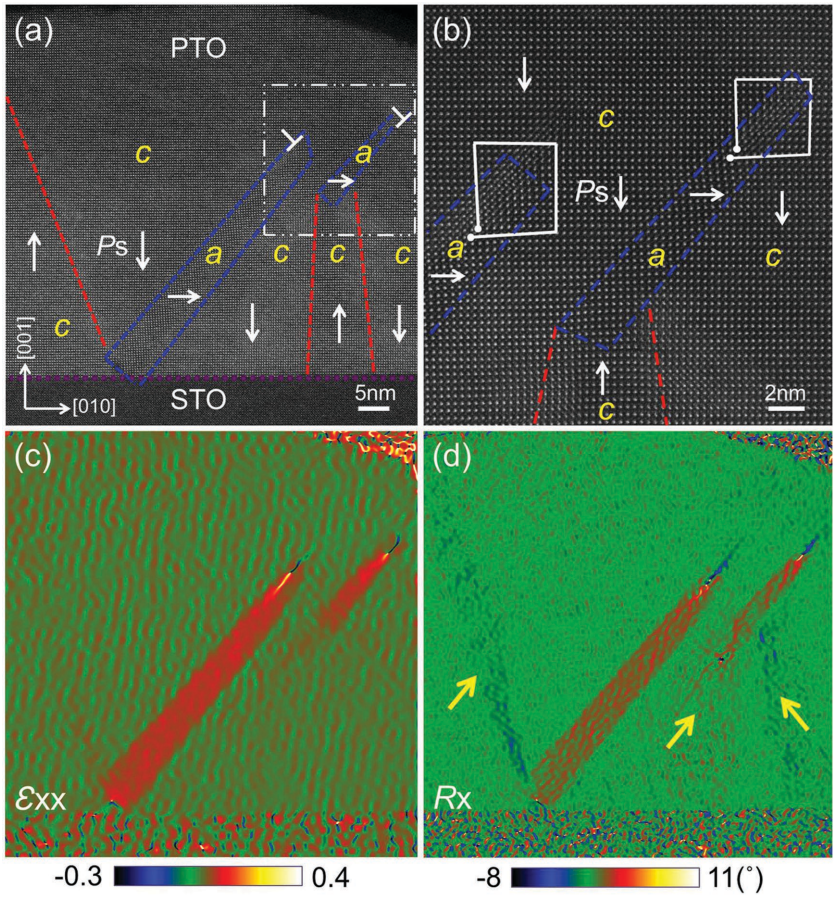

Figure 1. HAADF-STEM images and in-plane strain, lattice rotation analysis showing the domain configuration in PTO thin films resulted from interactions between 90°/180° domain walls and defects. a) A HAADF-STEM image shows the domain structure and dislocations. Navy blue and red dashed lines denote 90° and 180° domain walls; purple dotted line denotes STO/PTO interface; alphabet "*a*" and "*c*" denote *a*-domain and *c*-domain; white arrows denote polarization direction; "*T*" denotes dislocations with Burgers vector of $b = a[011]$. b) An enlarged high resolution HAADF-STEM image corresponding to the rectangular area in (a). White lines trace the Burgers circuits. c,d) In-plane strain (ε_{xx}) and lattice rotation (R_x) maps of (a). Yellow allows in (d) indicate 180° domain walls.

2. Results

2.1. The Formation of Metastable Domain Configurations

Metastable domain configurations, which are in apparent equilibrium state and capable to change to a more stable domain pattern, are recognized resulting from interactions between dislocations and 90°/180° domain walls. **Figure 1** shows a typical example of metastable domain configuration formation. Figure 1a is a low-magnification high resolution high angle annular dark field (HAADF) STEM image of the PTO film, which is recorded along [100] direction of both PTO and STO. 90° and 180° domain walls are identified as denoted by the blue and red dashed lines, respectively. Figure 1b is a magnified HAADF-STEM image corresponding to the rectangular area in Figure 1a, which shows the details of dislocations and their surrounding domain patterns. By drawing the Burgers circuits using white lines, we conclude that both dislocations feature Burgers vector of $b = a[011]$. Figure 1c,d are in-plane strain (ε_{xx}) and lattice rotation (R_x) mappings of (a). The *a*-domains, which are in red as shown in Figure 1c, can be identified due to the large in-plane lattice constant. Accordingly, the other areas are *c*-domains. The *a*-domains are also seen in red in Figure 1d. The fluctuation of the lattice rotation in *c*-domains is recognized, as indicated by yellow arrows. Such an in-plane lattice rotation is the character of a 180° domain wall, which agrees well with that in Figure 1a. Taken into account of the sign of lattice rotation, polarization directions in each area can be determined.[24,28–30] For example, a valley value of lattice rotation indicates the direction of spontaneous polarization (P_s) at the left side of a 180° domain wall is upward and vice versa. The P_s directions in *c*-domains deduced from lattice rotation mapping (Figure 1d) are shown in Figure 1a, as indicated by white arrows. Polarization directions in *a*-domain area are identified according to head-to-tail criterion which corresponds to a low energy state.[31] In this article, all the navy blue dashed lines denote uncharged 90° domain walls; red dashed lines denote 180° domain walls; purple dotted lines indicate heterogeneous interface between PTO film and STO substrate. "*a*," "*c*," and "T" denote *a*-domain, *c*-domain, and dislocation, respectively.

The stability of a domain pattern, especially a 180° domain wall, is of great importance because it is directly associated with the reliability of the data storage. To monitor the stability of the complex domain patterns where dislocation and 90°/180° domain walls coexist, as shown in Figure 1a, a second-round observations

are carried out 27 d after the first observations. It is found that the domain pattern changed dramatically to a more stable state. An appearance of a new 180° domain wall and an annihilation of the unstable 180° domain wall are observed. Moreover, the local *a*- and *c*-domains exhibiting reversal polarizations are identified. The directions of *P*s in each area can be further verified by the opposite direction of δ_{Ti},[26,29] where δ_{Ti} indicates Ti displacement vector with respect to the mass center of its four nearest Pb. More supplementary information on the development of domains is provided in Figures S1 and S2 in the Supporting Information.

Domain walls are important interfaces in ferroelectrics and play a significant role in the application of electronic device. Charged domain walls are known to exhibit unusual behaviors, for example, they promote local conduction in $Pb(Zr_{0.2}Ti_{0.8})O_3$.[9] The structures of such domain walls have been proved to be different from those of uncharged ones.[24,26] In the present work, head-to-head charged 90° domain walls are identified as a result of the interactions of 90°, 180° domain walls and lattice defects. **Figure 2**a is a HAADF-STEM image of the PTO film in which 90° and 180° domain walls can be identified and labeled as blue and red dashed lines. The enlarged HAADF-STEM image corresponding to the rectangular area in Figure 2a is shown in Figure 2b, which displays the dislocation and its surrounding domain configuration. Burgers circuit (white lines) in this image suggests that the dislocation feature the Burgers vector of $b = a[0\bar{1}\bar{1}]$. Figure 2c shows the in plane lattice strain (ε_{xx}) map corresponding to the area of Figure 2a. *a* – (in red) and *c* – (in blue) domains can be clearly revealed due to the larger in plane lattice constant of *a*-domain. Figure 2d shows the corresponding in plane lattice rotation (R_x) map. A red as well as a blue band are identified as indicated by yellow arrows, which correspond to the 180° domain walls. In Figure 2c,d, a frustration of 90° domain wall is observed as indicated by white arrows, which is determined to be head to head charged 90° domain wall and labeled by light blue dashed lines in Figure 2a. The detailed determination of this charged 90° domain wall is provided in the Supporting Information of this paper. An overview of the domain configurations shown in Figure 2a is similar to that observed in the polarization switching process reported by Gao et al.[32] This indicates that introducing lattice defects is an alternative approach to fabricate the novel charged domains walls. This domain pattern is also verified to be unstable. A second-round investigation which was carried out 27 d after the first reveals a new domain pattern (as shown in Figure S3, Supporting Information), where the charged 90° domain wall converts to the uncharged one and an annihilation of two 180° domain walls is identified.

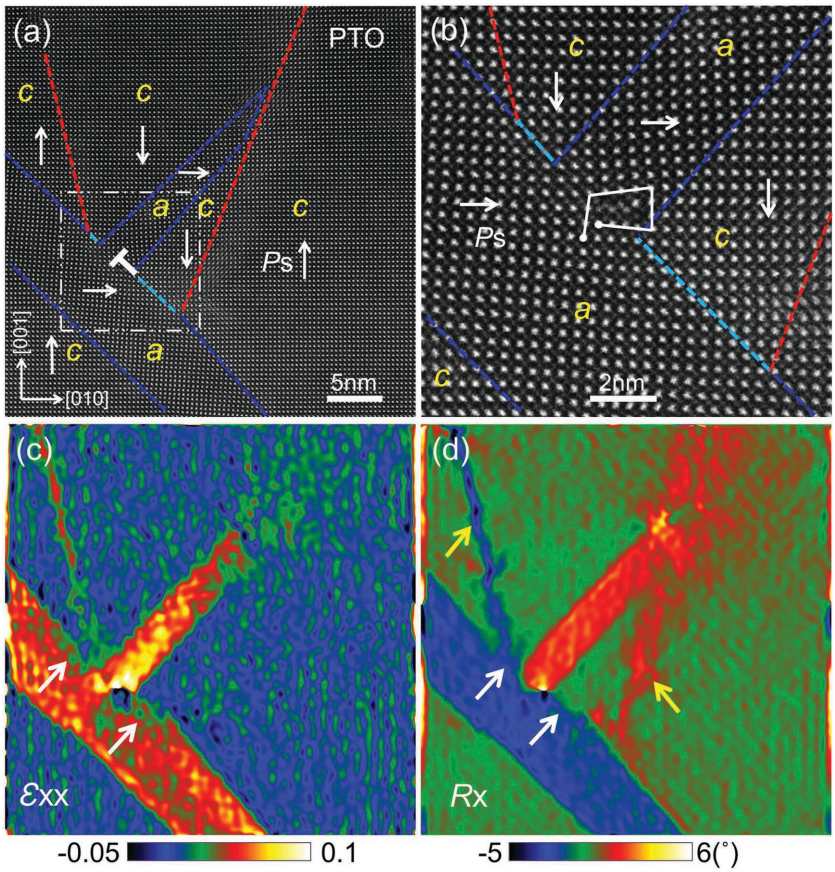

Figure 2. HAADF-STEM images and in-plane strain and lattice rotation maps showing the formation of 90° charged domain walls through lattice defects and 90°/180° domain walls interaction in PTO films. a) A high resolution HAADF-STEM image shows charged 90° domain wall formed in the area where 90°, 180° domain wall and dislocations intersect. Light blue dashed lines denote charged 90° domain walls; navy blue and red dashed lines denote 90° and 180° domain walls; purple dotted lines denote STO/PTO interface; alphabet "*a*" and "*c*" denote *a*-domain and *c*-domain; white arrows denote polarization direction; "T" denotes dislocations with $b = a[0\bar{1}\bar{1}]$. b) Enlarged HAADF-STEM images showing details of dislocation and its surrounding domain patterns corresponding to the rectangular area in (a). c,d) In-plane strain (ε_{xx}) and lattice rotation (R_x) maps of (a). White arrows in (c) indicate head to head 90° charged domain wall. Yellow arrows in (d) denote 180° domain walls.

Figure 3a–c shows that an interaction between domain walls and stacking fault can lead to the formation of head-to-head charged 90° domain wall, as indicated by light blue dashed lines. According to the in-plane strain (ε_{xx}) and lattice rotation (R_x) maps shown in Figure 3b,c, domains and their *P*s directions are revealed as shown in Figure 3a. In the present study, extensive observations indicate that a charged 90° domain walls frequently appear via the interaction of domain walls and lattice defects.

2.2. The Formation of Superdomains

A superdomain is composed of 90° stripe subdomains. Superdomains are interesting entities which may facilitate a great deal of exotic phenomena such as mesoscale ferroelectric flux-closure domain patterns.[33] Moreover, the Landau–Kittel scaling

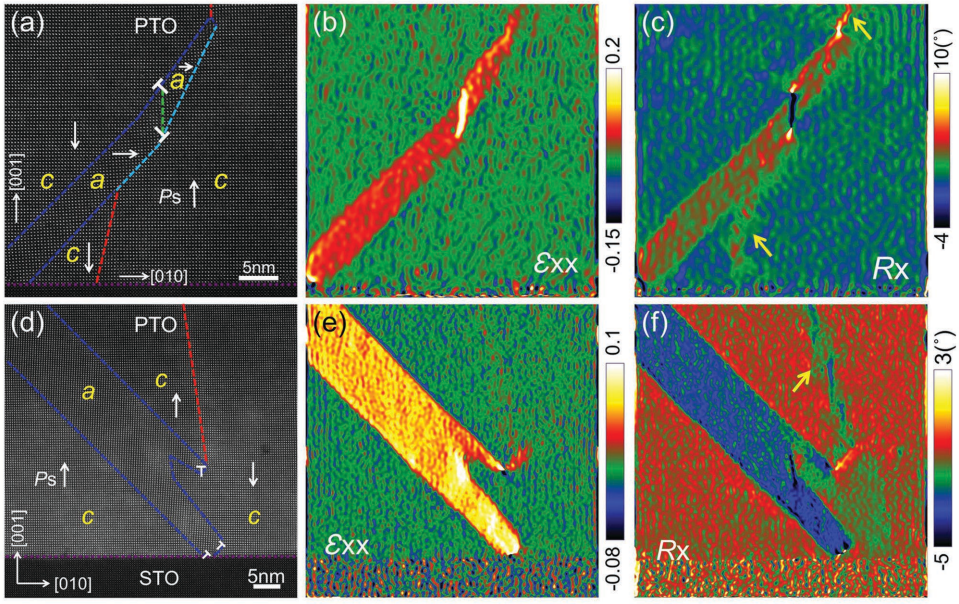

Figure 3. HAADF-STEM images and in-plane strain and lattice rotation maps showing (a–c) charged 90° domain wall and (d–f) superdomain structure formed due to 90°/180° domain walls interact with crystallographic defects. a) A HAADF-STEM image showing the domain configuration. Light blue dashed lines indicate charged 90° domain wall; green dashed line indicates stacking fault; "T" indicate partial dislocations with $b = 1/2a[0\bar{1}\,\bar{1}]$ and $1/2a[011]$; white arrows indicate polarization direction. b,c) In-plane strain (ε_{xx}) and lattice rotation (R_x) maps of (a). d) A high resolution HAADF-STEM image shows superdomain structure. White arrows denote polarization directions. "T" denote dislocations with $b = a[0\bar{1}0]$, $1/2a[0\bar{1}1]$, and $1/2a[0\bar{1}\,\bar{1}]$. e,f) In-plane strain (ε_{xx}) and lattice rotation (R_x) maps of (a). Yellow arrow denotes 180° domain wall.

law of these superdomains was observed.[34] In this study, we find that the formation of superdomains structure is also possible via the complex interactions in which dislocations, 90° domain walls, and 180° domain walls are involved. Figure 3d is a HAADF-STEM image and shows the domain configurations and *Ps* directions. Figure 3e,f displays the in-plane strain and lattice rotation analysis. It is seen that the strain in this superdomain is highly inhomogeneous. Such a special subdomain structure near the interface between the ferroelectric film and its substrate may result in a rather different polarization switching behaviors.[35]

2.3. The Formation of Specific Dislocations at the 90° Domain Walls

In the present study, the 90° domain walls usually emerge near the PTO/STO interface and extend into the PTO film. In addition, some specific dislocations are found to be regularly present along the 90° domain walls. Particularly, an unusual strain field of the dislocations in the middle of 90° domain wall is identified which is resultant from the coupling of the ferroelectric domain wall and the dislocation.

Figure 4a–f are HAADF-STEM images showing dislocations identified at the 90° domain walls near the PTO/STO interface. In the PTO films with the thickness of 40 nm, the *a*-domain is as narrow as 10–25 unit cells; while when the thickness reaches to 80 nm, some of the *a*-domains get to as wide as 25–45 unit cells. The narrow *a*-domains are usually accompanied with two kinds of dislocations. One is a perfect dislocation with Burgers vector of $b = a[0\bar{1}0]$ (type I), where an extra atomic planes is present in the substrate side, as shown in Figure 4a; while the other is partial dislocation pairs with the Burgers vector of $b = 1/2a[0\bar{1}1]$ or $1/2a[0\bar{1}\,\bar{1}]$ (type II) as shown in Figure 4b. In the case of wide *a*-domains (25 and 45 unit cells), the dislocation configurations are much more complex owing to the combination of dislocations with different types. Four dislocation configurations are identified in our experiments and shown in Figure 4c–f: (1) type II + type II (with the Burgers vector of $b = 1/2a[0\bar{1}\,\bar{1}]$), as shown in Figure 4c; (2) type II (with $b = 1/2a[0\bar{1}1]$) + $a[0\bar{1}0]$ + $a[001]$, as shown in Figure 4d; (3) type I + type II (with $b = 1/2a[0\bar{1}\,\bar{1}]$), as shown in Figure 4e; (4) type I + $a[0\bar{1}0]$ + $a[00\bar{1}]$, as shown in Figure 4f. The relationships between the thickness of PTO film, the width of *a*-domain, and dislocation patterns of *a*-domains close to the interface are summarized in **Table 1**.

Dislocations are also observed in the middle of the 90° domain walls, as shown in **Figure 5**a–e. Dislocations with Burgers vectors of $b = a[010]$, $a[0\bar{1}0]$, $a[001]$, and $a[00\bar{1}]$, respectively, are identified. Moreover, the interaction between the 90° domain wall and the dislocation is found to result in an unusual strain state. Figure 5b shows two dislocations along the 90° domain wall, each of which features a Burgers vector of $b = a[0\bar{1}0]$. The dislocations in perfect crystal should have shown symmetric ε_{xx} strain field along the vertical direction. In other words, the lattices above the dislocation core are tensile and the lattices below the core are compressive.[36] However, when such a dislocation lies in the 90° domain wall as shown in Figure 5b, a 45° rotation of the in-plane strain field is observed. Such a rotation makes the in-plane strain field symmetric along the 90° domain wall, as seen in Figure 5c. Figure 5f is a HAADF-STEM image showing a dislocation with Burgers vector of $b = a[011]$

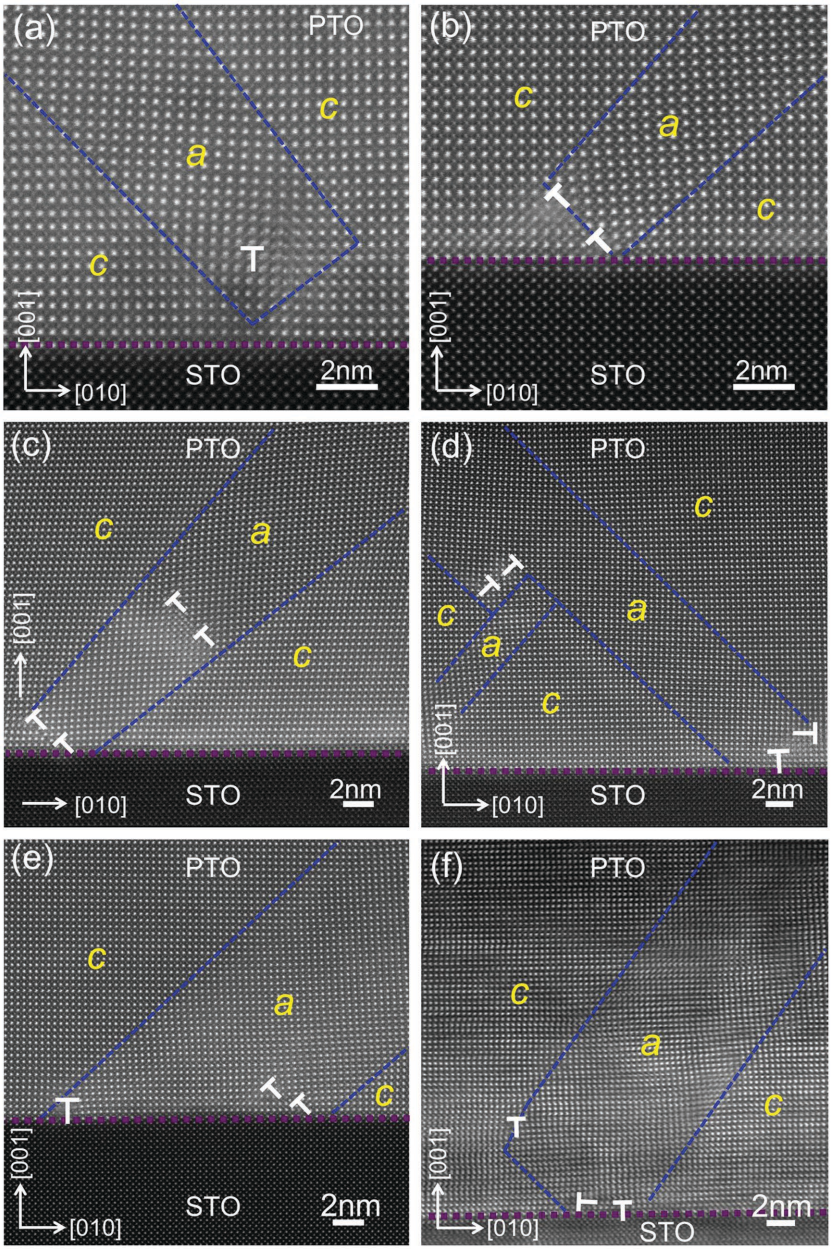

Figure 4. HAADF-STEM images showing dislocations at the starting position of *a*-domains near the PTO/STO interface. a,b) Two types of dislocation accompanied with narrow *a*-domains. a) One single dislocation with Burgers vector of $b = a[0\bar{1}0]$ (type I). b) Partial dislocation pairs with Burgers vectors of $b = 1/2a\,[0\,\bar{1}\,1]$ (type II). c–f) A combination of dislocations accompanied with wide *a*-domains. c) Dislocations with *b* = type II + type II (with $b = 1/2a[0\bar{1}\bar{1}]$). d) Dislocations with *b* = type II (with $b = 1/2a[0\bar{1}1]$) + $a[0\bar{1}0]$ + $a[001]$. e) Dislocations with *b* = type I + type II (with $b = 1/2a[0\bar{1}\bar{1}]$). f) Dislocations with $b = a[0\bar{1}0] + a[0\bar{1}0] + a[00\bar{1}]$.

at the end of 90° domain wall. In addition to the above observation, dislocations are also identified as a result of an interaction of two *a*-domains, or an interaction of 90° domain wall and a stacking fault. Such interactions and the resultant dislocations are observed in Figures 2a and 3a.

For tetragonal ferroelectrics PTO or $Pb(Zr_xTi_{1-x})O_3$ films, it was reported that if *a*-domains can move under applied electric field, ferroelectric and piezoelectric performance could be significantly improved.[37] However, these *a*-domains are usually clamped by interfacial dislocations and substrate.[20,37] Our results indicate that, dislocations may exist in anywhere along 90° domain wall. Their strain field, especially those along 90° domain wall, may exert great resistance to the movement of *a*-domains. These results will be helpful for understanding the polarization switching behaviors of ferroelectrics and the relevant piezoelectric properties.

3. Discussion

The polarization direction of a ferroelectric is switchable under an applied electric field, which allows ferroelectrics useful in high density nonvolatile memories. However, a written polarization is usually unstable due to either strain or build-in electric field induced elastic or electrostatic energy instability. This makes ferroelectric polarizations suffer from a potentially gradual back switching and leads to retention failure.[38,39] Lattice defects such as dislocations or stacking faults are known to have great impacts on the dynamics of domain switching.[11] The influences of defects on the formation of a domain pattern as well as domain relaxation process are also of great importance when the reliability of data storage is taken into account. Nevertheless, they are not well investigated so far in experiments. Our results shown in Figures 1, 2, 3 indicate that an interaction between domain walls and defects in the PTO film leads to metastable domain configurations. These phenomena may result from the pinning effect of defects which are likely to hinder the extending of a domain wall along the direction it supposed. These metastable domain patterns are prone to transform into a steady state on certain conditions, which may result in a data storage failure of ferroelectric memories. In addition, previous piezoresponse force microscopic studies indicated that a charged 90° domain wall, as that shown in Figure 2, could also reverse the switched 180° domain wall and result in a data loss as time elapsed.[40]

To better understand why *a*-domains usually appear along with dislocations, here we take the crystallographic information into account. For PTO/STO system, STO exhibits a cubic symmetry with lattice constant of a_{STO} = 3.905 Å; while PTO is tetragonal with the lattice constants of a_{PTO} = 3.899 Å and c_{PTO} = 4.153 Å. The lattice constant of STO is nearly identical to the "*a*" parameter of PTO. So if *c*-domain PTO is grown on a STO substrate, there is almost no mismatch. However, if *a*-domain PTO on a STO substrate,

Table 1. Relationship of the thickness of PTO films, width of *a*-domains and type of dislocations at the 90° domain walls near the PTO/STO interface.

Thickness of PTO	Width of *a*-domain	Type of dislocations
40 nm	10–25 unit cell	$a[0\bar{1}0]$ or $b = 1/2a[0\bar{1}1]$*2 or $1/2a[0\bar{1}\bar{1}]$*2
80 nm	10–25 unit cell	$a[0\bar{1}0]$ or $b = 1/2a[0\bar{1}1]$*2 or $1/2a[0\bar{1}\bar{1}]$*2
	25–45 unit cell	$1/2a[0\bar{1}\bar{1}]$*2 + $1/2a[0\bar{1}\bar{1}]$*2; or $1/2a[0\bar{1}1]$*2 + $a[0\bar{1}0]$ + $a[001]$; or $b = 1/2\ a[0\bar{1}\bar{1}]$*2 + $a[0\bar{1}0]$; or $a[0\bar{1}0]$ + $a[0\bar{1}0]$ + $a[00\bar{1}]$;

there is a large lattice mismatch. Such a lattice mismatch can be calculated according to the following equation

$$f = \frac{c(\mathrm{PTO}) - a(\mathrm{STO})}{(c(\mathrm{PTO}) + a(\mathrm{STO}))/2} \times 100\% \approx 6\% \quad (1)$$

Owing to this mismatch, every 16 *a*-domain unit cells correspond to one dislocation with Burgers vector $b = a[0\bar{1}0]$. Here the number 16 is derived from b/f (=1/0.06 ≈ 16). It is expected that more dislocations appear as the width of *a*-domain increases. In addition to the lattice mismatch, the twin relationship of 90° domain wall can also lead to a height difference of (001) lattice plane in two sides of an *a*-domain in the vertical direction, and such a height difference favors the formation of dislocations with Burgers vectors of $b = a[001]$ (or $a[00\bar{1}]$), as schematically illustrated in **Figure 6**a. Given the substrate is rigid, the height difference (h) between the two sides of an *a*-domain is

$$h = N \times c \times \sin\theta \quad (2)$$

Here, θ is lattice rotation angle between (010) plane of *a*-domain and (001) plane of *c*-domain. N is the number of *a*-domain unit cells. "*c*" is the lattice constant of PTO along [001]. It can be calculated by

$$\theta = 90^\circ - 2\tan^{-1}(a/c) \approx 3.6^\circ \quad (3)$$

when $N \times c \times \sin\theta = c$, N unit cells of *a*-domain is supposed to facilitate the formation of a dislocation with Burgers vector $b = a[001]$, then N can be calculated to be

$$N = 1/(\sin\theta) \approx 16 \quad (4)$$

Thus the larger difference in height induced by wider *a*-domain will facilitate the formation of more dislocations with Burgers vector of $b = a[001]$.

For the *a*-domain with a width of 16 unit cells, the appearance of dislocations with Burgers vector of $a[0\bar{1}0]$ result from the relaxation of lattice mismatch and the dislocations with Burgers vector of $a[001]$ are from the relaxation of the height mismatch. Moreover, the interaction of these two kinds of dislocations gives rise to the dislocations with Burgers vector of $b = a[0\bar{1}\bar{1}]$. However, the dislocation with Burgers vector of $a[0\bar{1}0]$ is found more often than $a[001]$ dislocation. For example, for the narrow *a*-domain, dislocations with Burgers vector not only $a[0\bar{1}\bar{1}]$ but also $a[0\bar{1}0]$ are observed. To explain this

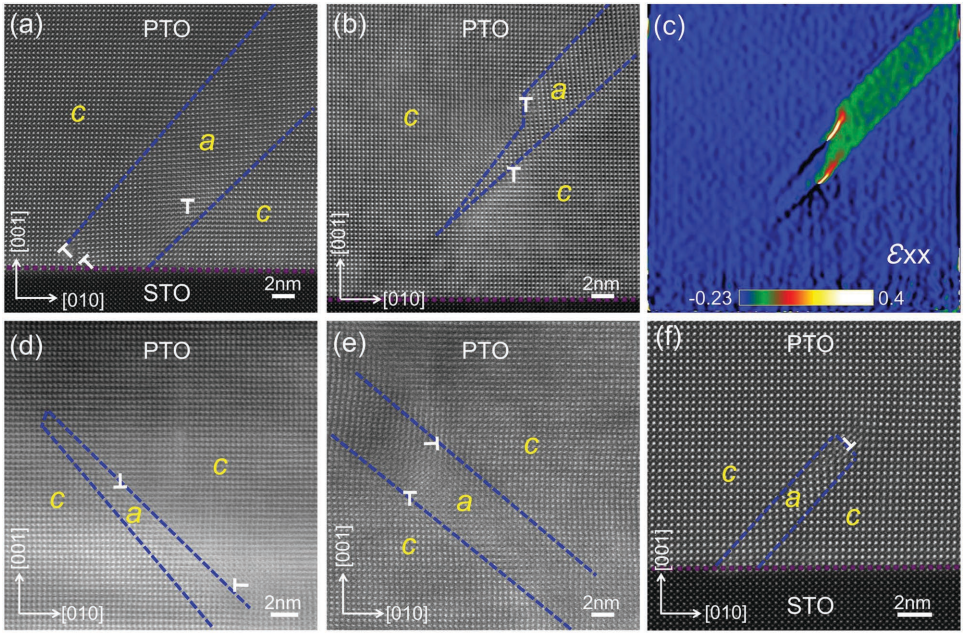

Figure 5. HAADF-STEM images showing dislocations in the middle and at the end of 90° domain walls. a,b,d,e) High resolution HAADF-STEM images showing dislocations in the middle of *a*-domains. a) One dislocation with $b = a[0\bar{1}0]$. b) Two dislocations with $b = a[0\bar{1}0]$. c) In-plane strain mapping of (b), showing the dislocation strain field along 90° domain wall. d) Two dislocations with $b = a[010]$ and $b = a[00\bar{1}]$. e) Two dislocations with $b = a[0\bar{1}0]$ and $b = a[001]$. f) A HAADF-STEM image showing a dislocation with Burgers vector $b = a[011]$ at the end of *a*-domain.

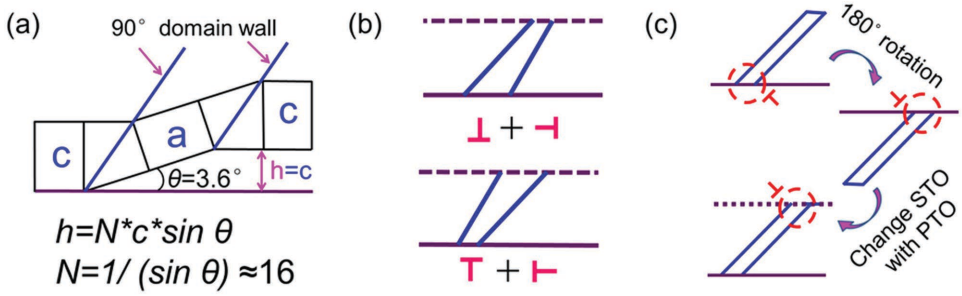

Figure 6. Schematic illustrations showing the formation of dislocations at the starting, in the middle and at the end of 90° domain walls. a) Formation of a dislocation with Burgers vector $b = a[00\bar{1}]$ (or $a[001]$) at the starting position of 90 ° domain wall. b) Schematic illustration of dislocation formed in the middle of *a*-domains. c) Schematic illustration showing relationship between dislocations at the starting position and at the end of *a*-domain.

phenomenon, dynamic process should be taken into account. For dislocations with $b = a[0\bar{1}0]$, previous studies usually ascribed its appearance to the interface mismatch,[20,41] and the strain field of this misfit dislocations eventually promote the formation of *a*-domain. Such dislocation and *a*-domain have a pinning effect on each other, so this kind of dislocations is easier to be reserved. However, for dislocation with $b = a[001]$, its formation is supposed to be a result of strain releasing in vertical direction when cooling, which rely severely on dynamic process of film growth, so this kind of dislocation is more difficult to form compared with $a[0\bar{1}0]$ dislocation.

Four kinds of dislocations formed in the middle of 90° domain walls are supposed to be a result of the width changing of the *a*-domains. Figure 6b schematically illustrates the correspondence of the specific dislocations with the width of *a*-domains.

Dislocations formed at the end of 90° domain wall (or *a*-domain) are also identified. Figure 6c is a schematic illustration showing the geometrical relationship between dislocations at the starting and at the end of *a*-domain. The geometric relationship indicates that these dislocations are of the same kind but with opposite Burgers vectors.

Dislocations are generally believed to deteriorate the physical properties of ferroelectric materials,[11,18,19] and defect-free $PbZr_{0.2}Ti_{0.8}O_3$ film with 90 nm thickness was grown by tuning the growing parameters in a pulsed laser deposition.[42] However, defects in ferroelectrics are not always undesired. In tetragonal ferroelectrics, it was reported that the interfacial dislocation may facilitate the formation of 90° domain wall,[20] and the 90° domain walls in $PbZr_{0.2}Ti_{0.8}O_3$ could further contribute to the dielectric property.[43] This suggests that dielectric property could be modified by controlling dislocations. Moreover, recent phase-field simulations reveal that dislocation walls in a PTO single crystal could improve the ferroelectric properties.[12] Furthermore, a study on the dislocations in perovskite oxide $Nd_{0.35}Sr_{0.65}MnO_3$ thin film grown on STO substrate reveals that the 1D electron chains were created by misfit dislocations strain field.[44] These phenomena stimulate experiment explorations of defect-induced novel properties in ferroelectrics.

4. Conclusion

The spatial coupling of the ferroelectric domain walls and the crystallographic defects in the PTO films grown on STO(001) substrate is investigated by means of aberration-corrected STEM. We find that the interactions of domain walls with lattice defects may lead to various metastable domain structures such as polarization unstable *a*- and *c*-domains, charged 90° domain wall, and superdomains. In addition, along the 90° domain walls we identify specific kinds of dislocations whose Burgers vectors are highly dependent on the width of *a*-domain. By digitizing the atomic-scale STEM images, we extract the strain fields of both the edge dislocations and the 90° domain walls and we find the variety of the strain fields resulting from the interaction between them. The present study is expected to be helpful for understanding the ferroelectric and piezoelectric properties of low-dimensional ferroelectric films.

5. Experimental Section

The PTO films with the thickness of 40 and 80 nm, respectively, were deposited on STO(001) substrate by pulsed laser deposition technique. The KrF (λ = 248 nm) excimer with a laser energy density of 2 J cm^{-2} was used. Prior to deposition, the substrate was heated to 750 °C and maintained for 5 min to clean the substrate surface and the target was presputtered for 30 min to make sure their surfaces were clean. When depositing PTO films, the substrate temperature was maintained at 650 °C. An oxygen pressure of 20 Pa and a laser repetition rate of 5 Hz were used. After deposition, the film was annealed in an oxygen pressure of 5 × 10^4 Pa at 650 °C for 10 min, and then cooled down to room temperature with a cooling rate of about 5 °C min^{-1}. The STEM specimens were prepared by slicing, grinding, dimpling, and finally ion milling. A Gatan PIPS 691 was used for the final ion milling. HAADF-STEM images were recorded using aberration-corrected scanning transmission electron microscopes (FEI Cubed Titan G2 60-300kV Transmission electron microscope) and Tecnai G2 F30 transmission electron microscopes. Strain analyses were based on geometry phase analysis,[45] which was carried out using Gatan Digital Micrograph software.

Supporting Information

Supporting Information is available from the Wiley Online Library or from the author.

Acknowledgements

This work was supported by the National Natural Science Foundation of China (Nos. 51231007, 51571197, 51501194, and 51521091) and

National Basic Research Program of China (2014CB921002). Y.-L.-T. acknowledges the IMR SYNL-T.S. Kê Research Fellowship and the Youth Innovation Promotion Association CAS (No. 2016177). The authors are grateful to B. Wu and L. X. Yang of this laboratory for their technical support on the Titan platform of G2 60-300kV aberration-corrected scanning transmission electron microscope.

Received: April 25, 2016
Revised: June 10, 2016
Published online:

[1] H. W. Jang, D. A. Felker, C. W. Bark, Y. Wang, M. K. Niranjan, C. T. Nelson, Y. Zhang, D. Su, C. M. Folkman, S. H. Baek, S. Lee, K. Janicka, Y. Zhu, X. Q. Pan, D. D. Fong, E. Y. Tsymbal, M. S. Rzchowski, C. B. Eom, *Science* **2011**, *331*, 886.
[2] A. Ohtomo, H. Y. Hwang, *Nature* **2004**, *427*, 423.
[3] J. Mannhart, D. H. A. Blank, H. Y. Hwang, A. J. Millis, J. M. Triscone, *MRS Bull.* **2008**, *33*, 1027.
[4] N. Reyren, S. Thiel, A. D. Caviglia, L. F. Kourkoutis, G. Hammerl, C. Richter, C. W. Schneider, T. Kopp, A. S. Ruetschi, D. Jaccard, M. Gabay, D. A. Muller, J. M. Triscone, J. Mannhart, *Science* **2007**, *317*, 1196.
[5] A. Tsukazaki, A. Ohtomo, T. Kita, Y. Ohno, H. Ohno, M. Kawasaki, *Science* **2007**, *315*, 1388.
[6] T. Kimura, T. Goto, H. Shintani, K. Ishizaka, T. Arima, Y. Tokura, *Nature* **2003**, *426*, 55.
[7] H. Zheng, J. Wang, S. E. Lofland, Z. Ma, L. M. Ardabili, T. Zhao, L. S. Riba, S.R. Shinde, S. B. Ogale, F. Bai, D. Viehland, Y. Jia, D. G. Schlom, M. Wuttig, A. Roytburd, R. Ramesh, *Science* **2004**, *303*, 661.
[8] J. Guyonnet, I. Gaponenko, S. Gariglio, P. Paruch, *Adv. Mater.* **2011**, *23*, 5377.
[9] J. Seidel, L. W. Martin, Q. He, Q. Zhan, Y. H. Chu, A. Rother, M. E. Hawkridge, P. Maksymovych, P. Yu, M. Gajek, N. Balke, S. V. Kalinin, S. Gemming, F. Wang, G. Catalan, J. F. Scott, N. A. Spaldin, J. Orenstein, R. Ramesh, *Nat. Mater.* **2009**, *8*, 229.
[10] A. Bhatnagar, A. R. Chaudhuri, Y. H. Kim, D. Hesse, M. Alexe, *Nat. Commun.* **2013**, *4*, 2835.
[11] P. Gao, C. T. Nelson, J. R. Jokisaari, S. H. Baek, C. W. Bark, Y. Zhang, E. Wang, D. G. Schlom, C. B. Eom, X. Pan, *Nat. Commun.* **2011**, *2*, 591.
[12] H. H. Wu, J. Wang, S. G. Cao, T. Y. Zhang, *Appl. Phys. Lett.* **2013**, *102*, 232904.
[13] A. Kontsos, C. M. Landis, *Int. J. Solids Struct.* **2009**, *46*, 1491.
[14] A. Y. Emelyanov, N. A. Pertsev, *Phys. Rev. B* **2003**, *68*, 214103.
[15] S. P. Alpay, I. B. Misirlioglu, V. Nagarajan, R. Ramesh, *Appl. Phys. Lett.* **2004**, *85*, 2044.
[16] Y. Zheng, B. Wang, C. H. Woo, *J. Mech. Phys. Solids* **2007**, *55*, 1661.
[17] Y. Zheng, B. Wang, C. H. Woo, *Appl. Phys. Lett.* **2006**, *88*, 092903.
[18] M. W. Chu, I. Szafraniak, R. Scholz, C. Harnagea, D. Hesse, M. Alexe, U. Gosele, *Nat. Mater.* **2004**, *3*, 87.
[19] C. L. Jia, S. B. Mi, K. Urban, I. Vrejoiu, M. Alexe, D. Hesse, *Phys. Rev. Lett.* **2009**, *102*, 117601.
[20] T. Kiguchi, K. Aoyagi, Y. Ehara, H. Funakubo, T. Yamada, N. Usami, T. J. Konno, *Sci. Technol. Adv. Mat.* **2011**, *12*, 034413.
[21] D. Su, Q. P. Meng, C. A. F. Vaz, M. G. Han, Y. Segal, F. J. Walker, M. Sawicki, C. Broadbridge, C. H. Ahn, *Appl. Phys. Lett.* **2011**, *99*, 102902.
[22] M. W. Chu, I. Szafraniak, D. Hesse, M. Alexe, U. Gosele, *Phys. Rev. B* **2005**, *72*, 173112.
[23] Z. R. Dai, Z. L. Wang, X. F. Duan, J. M. Zhang, *Appl. Phys. Lett.* **1996**, *68*, 3093.
[24] C. L. Jia, S. B. Mi, K. Urban, I. Vrejoiu, M. Alexe, D. Hesse. *Nat. Mater.* **2008**, *7*, 57.
[25] C. L. Jia, K. W. Urban, M. Alexe, D. Hesse, I. Vrejoiu, *Science* **2011**, *331*, 1420.
[26] Y. L. Tang, Y. L. Zhu, Y. J. Wang, W. Y. Wang, Y. B. Xu, W. J. Ren, Z. D. Zhang, X. L. Ma, *Sci. Rep.* **2014**, *4*, 4115.
[27] W. Y. Wang, Y. L. Tang, Y. L. Zhu, Y. B. Xu, Y. Liu, S. Jagadeesh, X. L. Ma, *Adv. Mater. Interfaces* **2015**, *2*, 1500024.
[28] B. Meyer, D. Vanderbilt, *Phys. Rev. B* **2002**, *65*, 104111.
[29] Y. L. Tang, Y. L. Zhu, X. L. Ma, A. Y. Borisevich, A. N. Morozovska, E. A. Eliseev, W. Y. Wang, Y. J. Wang, Y. B. Xu, Z. D. Zhang, S. J. Pennycook. *Science* **2015**, *348*, 547.
[30] Y. L. Tang, Y. L. Zhu, X. L. Ma, *Ultramicroscopy* **2016**, *160*, 57.
[31] W. J. Merz, *Phys. Rev.* **1954**, *95*, 690.
[32] P. Gao, J. Britson, J. R. Jokisaari, C. T. Nelson, S. H. Baek, Y. R. Wang, C. B. Eom, L. Q. Chen, X. Q. Pan, *Nat. Commun.* **2013**, *4*, 2791.
[33] R. G. McQuaid, L. J. McGilly, P. Sharma, A. Gruverman, J. M. Greg, *Nat. Commun.* **2011**, *2*, 404.
[34] L. J. McGilly, J. M. Gregg, *Appl. Phys. Lett.* **2011**, *98*, 132902.
[35] P. Sharma, R. G. P. McQuaid, L. J. McGilly, J. M. Gregg, A. Gruverman, *Adv. Mater.* **2013**, *25*, 1323.
[36] J. P. Hirth, J. Lothe, *Theory of Dislocations*, 2nd ed., John Wiley & Sons Inc, New York, USA **1982**, p. 77.
[37] V. Nagarajan, A. Roytburd, A. Stanishevsky, S. Prasertchoung, T. Zhao, L. Chen, J. Melngailis, O. Auciello, R. Ramesh, *Nat. Mater.* **2003**, *2*, 43.
[38] P. Gao, C. T. Nelson, J. R. Jokisaari, Y. Zhang, S. H. Baek, C. W. Bark, E. Wang, Y. M. Liu, J. Y. Li, C. B. Eom, X. Q. Pan, *Adv. Mater.* **2012**, *24*, 1106.
[39] M. P. Cruz, Y. H. Chu, J. X. Zhang, P. L. Yang, F. Zavaliche, Q. He, P. Shafer, L. Q. Chen, R. Ramesh, *Phys. Rev. Lett.* **2007**, *99*, 217601.
[40] A. Roelofs, N. A. Pertsev, R. Waser, F. Schlaphof, L. M. Eng, C. Ganpule, V. Nagarajan, R. Ramesh, *Appl. Phys. Lett.* **2002**, *80*, 1424.
[41] S. Stemmer, S. K. Streiffer, F. Ernst, M. Ruhle, *Phys. Stat. Sol.* **1995**, *147*, 135.
[42] I. Vrejoiu, G. L. Rhun, L. Pintilie, D. Hesse, M. Alexe, U. Goesele, *Adv. Mater.* **2006**, *18*, 1657.
[43] J. Karthik, A. R. Damodaran, L. W. Martin, *Phys. Rev. Lett.* **2012**, *108*, 167601.
[44] C. P. Chang, M. W. Chu, H. T. Jeng, S. L. Cheng, J. G. Lin, J. R. Yang, C. H. Chen, *Nat. Commun.* **2014**, *5*, 3522.
[45] M. J. Hytch, E. Snoeck, R. Kilaas, *Ultramicroscopy* **1998**, *74*, 131.